NeuroImage: Clinical 28 (2020) 102479

Contents lists available at ScienceDirect

NeuroImage: Clinical

journal homepage: www.elsevier.com/locate/ynicl

In vivo microstructural heterogeneity of white matter lesions in healthy elderly and Alzheimer's disease participants using tissue compositional analysis of diffusion MRI data

Remika Mito [a,b,1,*], Thijs Dhollander [a,b,c,1], Ying Xia [d], David Raffelt [a], Olivier Salvado [d,e], Leonid Churilov [a,f], Christopher C. Rowe [a,f,g], Amy Brodtmann [a,b,h], Victor L. Villemagne [a,f,g], Alan Connelly [a,b]

[a] Florey Institute of Neuroscience and Mental Health, Melbourne, Victoria, Australia
[b] Florey Department of Neuroscience and Mental Health, University of Melbourne, Melbourne, Victoria, Australia
[c] Developmental Imaging, Murdoch Children's Research Institute, Melbourne, Victoria, Australia
[d] CSIRO, Health & Biosecurity, The Australian eHealth Research Centre, Brisbane, Queensland, Australia
[e] CSIRO Data61, Sydney, New South Wales, Australia
[f] Department of Medicine, Austin Health, University of Melbourne, Victoria, Australia
[g] Department of Molecular Imaging & Therapy, Centre for PET, Austin Health, Heidelberg, Victoria, Australia
[h] Eastern Clinical Research Unit, Monash University, Box Hill Hospital, Melbourne, Victoria, Australia

ARTICLE INFO

Keywords:
White matter hyperintensities
3-tissue
Heterogeneity
Diffusion MRI
Alzheimer's disease

ABSTRACT

White matter hyperintensities (WMH) are regions of high signal intensity typically identified on fluid attenuated inversion recovery (FLAIR). Although commonly observed in elderly individuals, they are more prevalent in Alzheimer's disease (AD) patients. Given that WMH appear relatively homogeneous on FLAIR, they are commonly partitioned into location- or distance-based classes when investigating their relevance to disease. Since pathology indicates that such lesions are often heterogeneous, probing their microstructure *in vivo* may provide greater insight than relying on such arbitrary classification schemes. In this study, we investigated WMH *in vivo* using an advanced diffusion MRI method known as single-shell 3-tissue constrained spherical deconvolution (SS3T-CSD), which models white matter microstructure while accounting for grey matter and CSF compartments. Diffusion MRI data and FLAIR images were obtained from AD (n = 48) and healthy elderly control (n = 94) subjects. WMH were automatically segmented, and classified: (1) as either periventricular or deep; or (2) into three distance-based contours from the ventricles. The 3-tissue profile of WMH enabled their characterisation in terms of white matter-, grey matter-, and fluid-like characteristics of the diffusion signal. Our SS3T-CSD findings revealed substantial heterogeneity in the 3-tissue profile of WMH, both within lesions and across the various classes. Moreover, this heterogeneity information indicated that the use of different commonly used WMH classification schemes can result in different disease-based conclusions. We conclude that future studies of WMH in AD would benefit from inclusion of microstructural information when characterising lesions, which we demonstrate can be performed *in vivo* using SS3T-CSD.

Abbreviations: AIBL, Australian Imaging Biomarkers and Lifestyle study of ageing; CSD, Constrained spherical deconvolution; CSF, cerebrospinal fluid; DTI, Diffusion tensor imaging; DWI, Diffusion-weighted imaging; FLAIR, Fluid-attenuated inversion recovery; FOD, Fibre orientation distribution; GM, Grey matter; HIST, HyperIntensity Segmentation Tool; NAWM, Normal-appearing white matter; SS3T-CSD, Single-shell 3-tissue constrained spherical deconvolution; T_C, Cerebrospinal fluid-like signal fraction; T_G, Grey matter-like signal fraction; T_W, White matter-like signal fraction; WM, White matter; WMH, White matter hyperintensities.

* Corresponding author at: Florey Institute of Neuroscience and Mental Health, 245 Burgundy Street, Heidelberg, Victoria 3084, Australia.
E-mail address: remika.mito@florey.edu.au (R. Mito).

[1] These authors contributed equally to this work.

https://doi.org/10.1016/j.nicl.2020.102479
Received 1 May 2020; Received in revised form 25 September 2020; Accepted 19 October 2020
Available online 26 October 2020

1. Introduction

Magnetic resonance imaging (MRI) enables us to probe the *in vivo* structure of the brain with high anatomical resolution, facilitating identification of brain abnormalities and diagnosis of neurological diseases. As MRI methods have vastly improved over the past few decades, resulting in a corresponding improvement in their clinical utility, we have grown somewhat accustomed to identifying specific MRI abnormalities, and often, to making assumptions about their underlying pathological changes. Indeed, it has become commonplace to identify MRI abnormalities, and to use them as biomarkers or imaging markers of known pathological or clinical correlates. However, not all MRI abnormalities are straightforward to interpret. One such MRI abnormality in which ambiguity remains, is the presence of white matter hyperintensities observed on T2-weighted MRI.

White matter hyperintensities (WMH) are commonly observed in elderly individuals, and can be identified on fluid-attenuated inversion recovery (FLAIR) images, where they appear as hyperintense regions within white matter. While FLAIR is useful for radiological identification of these lesions, it is non-specific in distinguishing between underlying pathological changes. Histopathological-imaging correlational studies in post-mortem brains have shown that WMH are characterised by a heterogeneous histological profile, including myelin pallor, myelin loss, axonal loss, gliosis and white matter infarction (Braffman et al., 1988; Fazekas et al., 1993; Gouw et al., 2008; Young et al., 2008; Schmidt et al., 2011a). Most of these histological changes are thought to be ischaemic in origin (Pantoni et al., 1996; Pantoni and Garcia, 1997; Topakian et al., 2010), and consequently, WMH have been proposed as a proxy measure for small vessel disease, and a surrogate endpoint for cerebrovascular clinical trials (Schmidt et al., 2004). While it may be a useful clinical surrogate, using global measures of WMH as a marker for small vessel disease disregards information about known pathological heterogeneity. Moreover, not all WMH observed on MRI have microangiopathic origin (Fazekas et al., 1993; McAleese et al., 2017), and different lesions may have distinct clinical and pathological correlates.

WMH have been shown for some time to be greater in volume and severity in Alzheimer's disease patients than in healthy elderly individuals (Rezek et al., 1987; Scheltens et al., 1992; Barber et al., 1999), and more recently, have been considered by some to be a core feature of Alzheimer's disease (Lee et al., 2016); however, the role of these lesions in contributing to Alzheimer's disease either through additive or interactive effects is not entirely understood. In the context of Alzheimer's disease, distinguishing between different types of WMH is particularly relevant, given that some lesions are believed to be more closely associated with the disease, whereas others are thought to be less deleterious, age-associated injuries (Brickman et al., 2015; McAleese et al., 2017).

In an attempt to distinguish between certain types of WMH, classification schemes are commonly adopted, differentiating these lesions based on their location, shape or size. Commonly, these classification schemes distinguish periventricular WMH from deep WMH, or distinguish confluent lesions from punctate lesions. However, classification schemes differ, and the same terms are often used to define WMH in a disparate manner (Kim et al., 2008). For instance, while many visual rating scales define periventricular WMH as those lesions that have continuity with the lateral ventricles (Fazekas et al., 1987; Coffey et al., 1990; de Leeuw et al., 2000), others classify periventricular lesions based on their distance from the ventricular surface (Wen and Sachdev, 2004; DeCarli et al., 2005), or their shape or size (Schmidt et al., 1992; Scheltens et al., 1993). Unsurprisingly, the clinical and pathological correlates of different classes of WMH appear variable, given the inconsistency among classification schemes (Van Straaten et al., 2006; Kim et al., 2008). Moreover, the use of categorical distinction to differentiate WMH has itself been criticised as somewhat arbitrary, as such classifications may not necessarily correspond to meaningful pathological differences (DeCarli et al., 2005).

In vivo methods that are able to identify and measure microstructural heterogeneity of these lesions could thus be highly valuable, given that they would likely reflect pathological differences among lesion types, above and beyond the binary identification of WMH that is possible with FLAIR. Imaging modalities that have been used to date to probe heterogeneity within lesions include magnetization transfer ratio (Spilt et al., 2006) and T1 relaxation time (Brex et al., 2000). One MRI approach that is particularly suited to probe tissue microstructure is diffusion MRI, or diffusion-weighted imaging (DWI). Signal intensity on diffusion MRI is sensitive to the microscopic diffusion of water, and can be used to study white matter fibre architecture *in vivo*. As such, it is potentially sensitive to microstructure within WMH. The ability to appropriately model white matter structures, however, depends upon the type of diffusion data acquired, and the methods used to model these diffusion data. Diffusion tensor imaging (DTI) (Basser et al., 1994) is commonly used to model white matter microstructure, and has been widely applied to investigate microstructural properties of WMH. While it is sensitive in detecting differences in WMH (Bastin et al., 2009; Maniega et al., 2015), there are well-known limitations to the DTI model that render it problematic when interpreting results, particularly when multiple fibre orientations are present (Le Bihan et al., 2006; Jones, 2010; Jones et al., 2013).

Constrained spherical deconvolution (CSD) is a method that enables modelling of white matter in the presence of multiple fibre orientations (Tournier et al., 2004, 2007), even when there are crossing fibre populations within a voxel, and thus offers a means to model complex white matter structures better than the DTI model. However, the ability of CSD to model white matter may be confounded in areas where there is partial voluming with other tissues, such as grey matter (GM) or cerebrospinal fluid (CSF). This issue can be overcome by modelling GM and CSF signal fractions, for example by using multi-shell multi-tissue CSD (Jeurissen et al., 2014). However, this requires multi-shell data, typically implying the additional use of low b-values, which introduces some amount of extra-axonal signal (Genc et al., 2020). Alternatively, a recently introduced variant of the CSD method, called single-shell 3-tissue CSD (SS3T-CSD) (Dhollander and Connelly, 2016a; Dhollander et al., 2016), is able to additionally estimate the GM and CSF compartments using single-shell diffusion data alone. In doing so, the effects of partial volume of non-white matter signal, which can otherwise result in overestimation of the white matter compartment, are minimised. More recently, SS3T-CSD has additionally been proposed as a means to provide insight into microstructural properties of pathological tissue (Dhollander et al, 2017). By characterising the diffusion signal obtained from tissue in terms of its relative composition of diffusion signal characteristics similar to those of the three distinct tissue types (i.e., those obtained from white matter, GM and CSF), this method can provide insight into the microstructural properties of different types of tissue. This could then be applied to probe the underlying diffusional characteristics of WMH, as pathological changes within these lesions could result in signal characteristics that deviate from normal white matter, enabling microstructural heterogeneity within these lesions to be potentially detected and characterised *in vivo*.

In this study, we sought to investigate WMH using SS3T-CSD in a cohort of Alzheimer's disease patients ($n = 48$) and healthy elderly control subjects ($n = 94$). Our aims were to investigate heterogeneity in the microstructural properties of these WMH *in vivo*, and to determine whether WMH exhibit distinct diffusional characteristics that would provide additional information to that obtained using conventional binary lesion classification schemes. Moreover, we were interested in determining whether multi-tissue diffusional characteristics of lesions could offer disease-relevant information in the context of Alzheimer's disease.

2. Materials and methods

2.1. Participants

Participants included in this study were recruited as part of the Australian Imaging, Biomarkers and Lifestyle (AIBL) study of aging, and consisted of patients with clinical Alzheimer's disease, and healthy elderly control subjects. Participants were classified into clinical groups according to AIBL criteria, and satisfied inclusion and exclusion criteria, as has been previously described (Ellis et al., 2009). Participants were included in this study if their MRI protocol included high b-value diffusion MRI, acquired at the Florey Institute of Neuroscience and Mental Health in Melbourne ($n = 149$). All participants also underwent an amyloid-β PET scan with ^{11}C-PIB (carbon-11-labelled Pittsburgh compound B), and were classified as amyloid-positive or -negative based on a mean standardised uptake value ratio (SUVR) cut-off value of 1.4, as previously described (Rowe et al., 2013). Participants who had a clinical diagnosis of Alzheimer's disease, but were amyloid-negative were excluded ($n = 3$). Participants were also excluded if they had incomplete demographic information ($n = 2$). FLAIR images were screened automatically for the presence of WMH. Subjects with substantial motion or intensity inhomogeneity artefacts on their FLAIR image were excluded from analysis, as automated segmentation of WMH on these subjects failed ($n = 2$). The final cohort included 142 subjects: 48 Alzheimer's disease and 94 healthy control subjects. All subjects provided informed written consent, and the study was approved by the ethics committee at Austin Health.

2.2. Image acquisition

MRI data were acquired for all subjects using a 3 T Siemens Tim Trio System (Erlangen, Germany), with a 12-channel head coil receiver. DWI

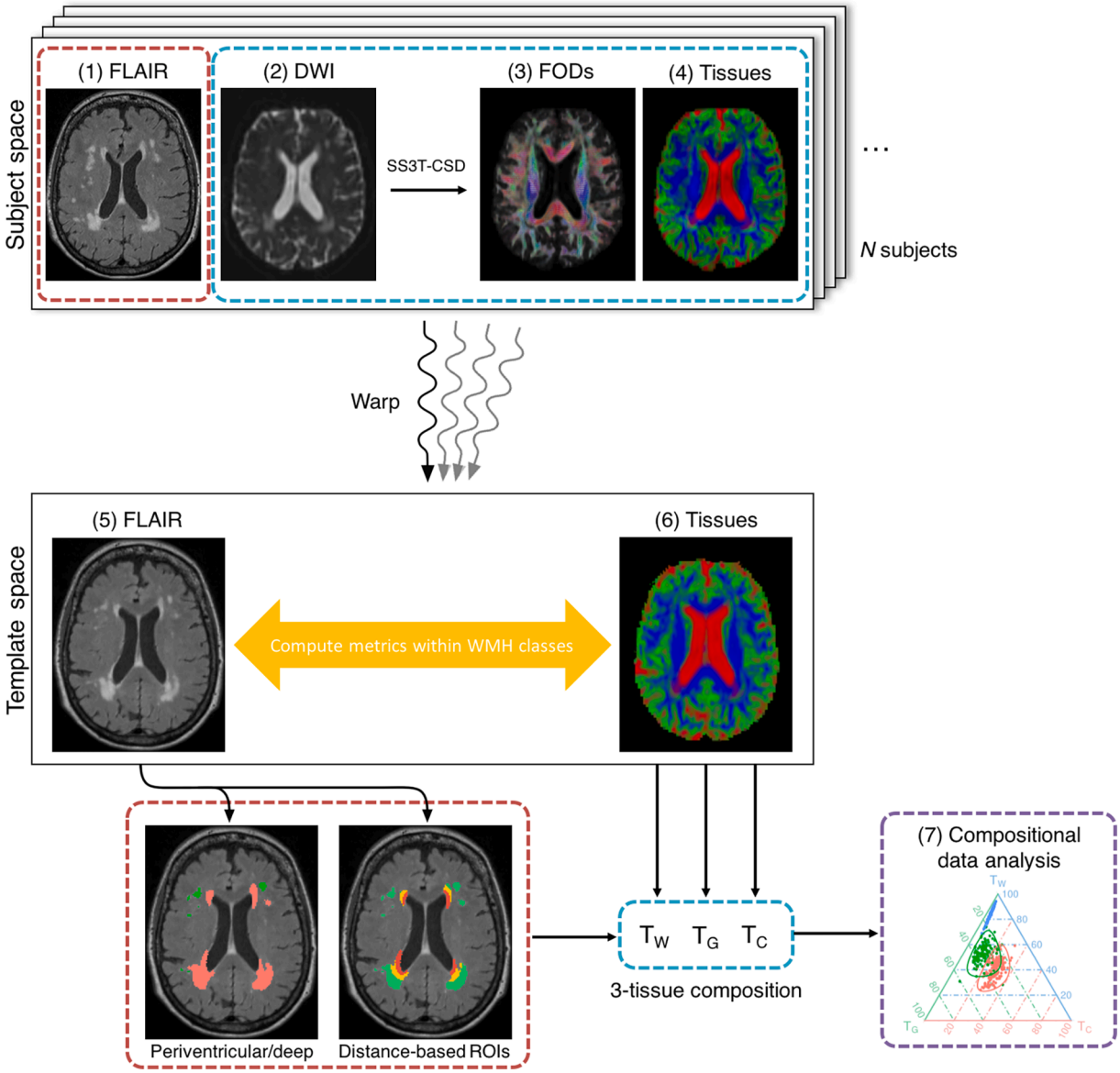

Fig. 1. Schematic figure showing the major steps involved in diffusional analysis of white matter hyperintensities. (1) FLAIR and (2) DWI data were obtained for each subject, and were motion corrected and preprocessed. Single-shell 3-tissue constrained spherical deconvolution (SS3T-CSD) was performed on the DWI data to obtain (3) fibre orientation distribution (FOD) functions for white matter, as well as for the grey matter and CSF compartments, enabling (4) tissue maps to be created. Each subject's images were warped to a common template space. Within each of the WMH classes obtained from classification schemes applied on (5) the FLAIR WMH segmentations, we then computed (6) the signal fractions obtained from the diffusion data (T_W, T_G, T_C). The 3-tissue profile for each of the WMH classes could then be analysed with (7) compositional data analysis (CoDA).

data were collected using echo planar imaging (EPI) with the following parameters: TR/TE = 9200/112 ms, 2.3 mm isotropic voxels, 128 × 128 acquisition matrix, acceleration factor = 2, diffusion-weighted images for 60 different gradient directions (b = 3000 s/mm^2) and 5 volumes without diffusion-weighting (b = 0 s/mm^2). FLAIR images were collected with the following parameters: 176 axial slices, voxel size 0.9 × 0.98 × 0.98 mm^3, repetition time/echo time = 6000/420 ms, inversion time = 2100 ms, flip angle = 120°). A 3D MPRAGE (magnetization prepared rapid acquisition gradient echo) image (voxel size 1.2 × 1 × 1 mm^3, repetition time/echo time = 2300/2.98, flip angle = 9°) was also obtained for each subject, and used to compute intracranial volume using SPM8 software. Scan times were approximately 9 min for DWI, 7 min for FLAIR, and 10 min for 3D MPRAGE. FLAIR and DWI data were then preprocessed and analysed using MRtrix3 (Tournier et al., 2019) as described in the following sections, and as summarised in Fig. 1.

2.3. Image preprocessing

Preprocessing of diffusion-weighted images included denoising of data (Veraart et al., 2016), eddy-current distortion correction and motion correction (Andersson and Sotiropoulos, 2016), bias field correction (Tustison et al., 2010), and up-sampling resulting in 1.15 × 1.15 × 1.15 mm^3 isotropic voxels (Raffelt et al., 2012a). Gibbs deringing was not performed on this dataset. Intensity normalization across subjects was performed by deriving scale factors from the median intensity in select voxels of white matter, grey matter, and CSF in b = 0 s/mm^2 images, then applying these across each subject image.

Following these initial preprocessing steps, group averaged response functions for WM, GM, and CSF were obtained from select voxels within the data themselves using an unsupervised method (Dhollander et al., 2019), which excludes voxels located in lesions (Dhollander et al., 2018). WM fibre orientation distribution (FOD) functions, as well as GM and CSF compartments were computed using Single-Shell 3-Tissue CSD (SS3T-CSD) (Dhollander and Connelly, 2016a) in MRtrix3Tissue (https://3Tissue.github.io). While the mechanism of the SS3T-CSD method is described elsewhere (Dhollander and Connelly, 2016a) and the implementation is open source, we provide a brief description of the assumptions, as compared to multi-shell multi-tissue CSD (MSMT-CSD; Jeurissen et al., 2014). The SS3T-CSD method estimates in each voxel an anisotropic WM FOD from the DWI data that is less influenced by isotropic GM and CSF signal contributions by separating the latter signals into their own compartments. Similar to MSMT-CSD, this signal representation assumes a unique anisotropic single-fibre WM response function and unique isotropic GM and CSF response functions across the brain. Whereas MSMT-CSD requires multi-shell data to be able to estimate 3 tissue compartments (Jeurissen et al., 2014), SS3T-CSD only requires single-shell + b = 0 s/mm^2 data due to its bespoke iterative estimation strategy (Dhollander and Connelly, 2016a). Interestingly, this allows it to *not* have to rely on the same aforementioned assumptions for lower b-values (between b = 0 s/mm^2 and the largest b-value available in the data), both in isolation as well as across the contrast of signal decay. Finally, using SS3T-CSD, the resulting WM FOD is then also *not* weighted by the signal from lower b-value(s), and consequently the resulting apparent fibre density is less biased by extra-axonal signal and more specifically sensitised to intra-axonal volume. The latter is consistent with recent findings by Genc et al., (2020), where use of higher b-values was found to result in more accurate estimates of WM fibre density using simulated data, and corroborated by their *in vivo* studies.

FLAIR images and MPRAGE images were also bias field-corrected (Tustison et al., 2010). EPI susceptibility distortion correction of diffusion-weighted images was performed in conjunction with MPRAGE motion correction, using a registration-based method guided by a pseudo T1-contrast, which was estimated from the SS3T-CSD result (ie. the 3-tissue compartments) (Dhollander and Connelly, 2016b).

Spatial correspondence across subjects was achieved by first computing a group-specific population template via an iterative registration and averaging approach (Raffelt et al., 2011) using the white matter FOD images from 30 subjects from the study cohort. Each subject's FOD image was then registered to the template via a FOD-guided non-linear registration (Raffelt et al., 2011, 2012b). FLAIR images were also corrected for motion (via registration to each subject's MPRAGE image using ANTS (Avants et al., 2014)) and warped to the population template space, along with the WMH segmentations that were obtained from these FLAIR images (see next section).

2.4. Lesion segmentation and classification

WMH segmentations were performed automatically using the HyperIntensity Segmentation Tool (HIST), which has previously been trained on the AIBL cohort (Manjón et al., 2018). This automated tool segments WMH from 3D FLAIR images based on an ensemble of neural network classifiers. WMH segmentations were visually inspected for quality assurance. Given the variability of definitions used for classification of WMHs in the literature, segmented WMH were then classified according to 2 different sets of criteria.

Firstly, WMH were classified either as "periventricular" or "deep" lesions, based on their distance and confluence with the lateral ventricles, using confluence-based periventricular WMH criteria. WMH lesion volumes were classified as periventricular if the minimum distance of a continuously connected lesion volume from the lateral ventricles was less than 5.0 mm, or if the average distance of a continuous lesion volume was less than 20.0 mm from the lateral ventricles. WMH were otherwise classified as deep. Here, lesions were categorised on each individual's FLAIR image, and then transformed to template space.

Secondly, a classification of each WMH voxel was performed separately based on its distance from the ventricles, regardless of continuity of a lesion (see Fig. 2), extending the distance-based classification scheme described by DeCarli et al. (2005). A ventricular mask was obtained by intensity thresholding the average FLAIR image across all subjects in template space, and manually removing any CSF voxels that were not within the lateral ventricles. Three regions-of-interest were then defined by dilating the ventricular mask to an area that included anything 10 mm or less from the lateral ventricles in all directions. WMH voxels falling within this region were classified as Region 1, regardless of whether they had contiguous WMH voxels that extended beyond this region. A second region (Region 2) was defined by further dilating the first region to obtain an area between 10 mm and 20 mm from the lateral ventricles. The third region (Region 3) consisted of all remaining white matter beyond 20 mm from the lateral ventricles.

A normal-appearing white matter (NAWM) mask was defined for each subject in template space. A WM segmentation was obtained from each subject's T1 image in template space, using FSL FAST (Zhang et al., 2001). The WMH for each subject were subtracted from that subject's WM segmentation, and the remaining NAWM mask was subsequently eroded by one voxel in three dimensions to ensure that voxels within this mask represented normal-appearing WM only.

2.5. Representing the composition of WMH and NAWM as 3-tissue diffusion signal fractions

The WM, GM and CSF compartments were obtained from SS3T-CSD as described above. As CSD techniques typically operate directly on the *absolute* diffusion-weighted signal, these compartments are also directly proportional to the *absolute* amount of diffusion-weighted signal attributable to each of these tissue types in each voxel. In previous work, it was found that certain microstructural aspects of WM pathology result in diffusion-weighted signals akin to those represented by the response functions measured from GM and CSF (Dhollander et al, 2017). In this context, these were referred to as "GM-like" and "CSF-like" (diffusion-weighted) signals. In the present work, we intended to study the *relative* makeup of the diffusion-weighted signal in terms of WM-, GM- and CSF-

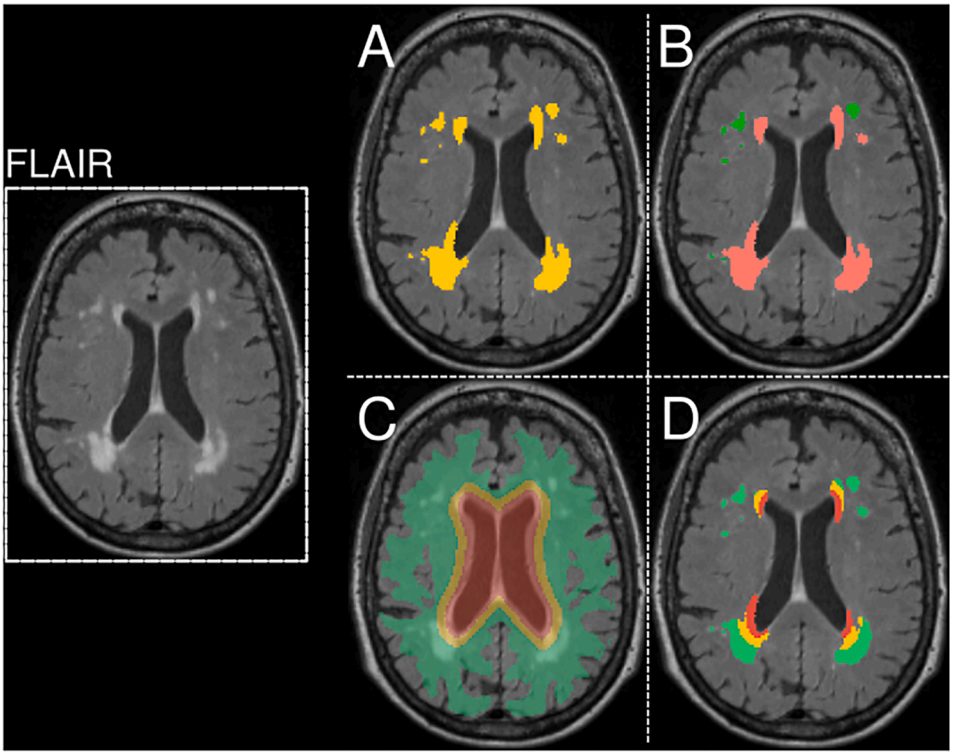

Fig. 2. White matter hyperintensity segmentation and classification schemes. White matter hyperintensities were automatically segmented from FLAIR MRI. A single axial slice of the FLAIR image is shown on the left for a given subject in template space. (A) The WMH segmentation for this subject is shown in yellow. (B) An example of the periventricular/deep classification scheme is shown for the WMH in a given subject. WMH were classified as "periventricular" if the minimum distance of a lesion volume from the lateral ventricles was<5.0 mm in subject space or if the average distance of a continuous lesion was<20.0 mm from the lateral ventricles. WMH were otherwise classified as "deep". (C) Regions of interest were defined by repeatedly dilating a ventricular mask obtained from the population template brain. The first region (Region 1) is shown in red, and included an area 10 mm or less from the lateral ventricles in all directions. Region 2 is shown in yellow, and was defined by further dilating Region 1 to obtain an area between 10 mm and 20 mm from the lateral ventricles. Region 3, shown in green, consisted of all remaining white matter beyond 20 mm from the lateral ventricles. (D) Lesions were classified into these distance-based classes according the Region with which they overlapped. (For interpretation of the references to colour in this figure legend, the reader is referred to the web version of this article.)

like tissue signal *fractions*. To distinguish these from the *absolute* signals, we refer to the 3-tissue signal *fractions* as T_W, T_G and T_C respectively.

While the WM, GM and CSF response functions are estimated from voxels containing conservative samples of these three tissue types, it should be noted that the signal fractions (T_W, T_G, and T_C) should not be interpreted as literally reflecting these three tissue types, for example, in a biological, chemical or functional way. Rather, T_W, T_G, and T_C are then used to describe the diffusion signal characteristics of WMHs. In other words, the SS3T-CSD result is in this context employed as a *diffusion signal representation* rather than a biophysical model of microstructure. For example, an increase in the CSF-like signal fraction is compatible with an increased free water content, but this does not have to be accompanied by the same chemical makeup as CSF. Likewise, an increase in the GM-like signal fraction does not necessarily imply a biological resemblance to cortical or other genuine GM, but might be compatible with an increased presence of glial or other cells. From a diffusion signal representation point of view, a shift from WM-like towards more GM-like diffusion signal rather indicates increased diffusion isotropy and increased diffusivity. A shift towards more CSF-like signal, on the other hand, indicated a far greater increase in diffusivity, relatively speaking.

To obtain T_W, T_G and T_C for each WMH category and NAWM per subject, the absolute WM-like, GM-like and CSF-like signal were computed over each WMH category, and the resulting triplet of absolute signals normalised to sum to one. The resulting 3-tissue composition of each WMH category and NAWM for each subject included in the analysis was plotted on a ternary plot. Ternary plots were created using the *ggtern* package in R (Hamilton, 2018), enabling easy visualisation of the 3-tissue profile of the WMH categories and NAWM regions. A schematic showing how the ternary space broadly relates to the diffusion signal properties is provided in the Supplementary Material (Fig. S1).

2.6. Investigating WMH and NAWM with FA

The most commonly used method to date to probe white matter changes using diffusion MRI is using tensor-derived metrics, such as fractional anisotropy (FA) and mean diffusivity (MD). As such, in addition to the 3-tissue profiles that constitute the main result of this study, FA and MD analyses are provided for reference. The detailed methodology, along with the results, can be found in the Supplementary Material.

2.7. Statistical analysis

Demographic variables and WMH volumes were compared between the two clinical groups. We used *t*-tests and χ^2 tests to compare age, sex, and intracranial volume. WMH volumes were compared between groups by performing ANCOVAs, including age and intracranial volume as covariates. Given that the distribution of WMH volumes across subjects is right-skewed, we performed a cubic root transformation to all WMH volumes to normalise the distribution. Bonferroni-corrected *P*-values were used to determine statistical significance.

In this study, we were most interested in determining whether there was heterogeneity across different WMH classes or types, and as such, for subsequent analyses, we compared the 3-tissue profiles between different classes of WMH and NAWM, across all subjects, combining the Alzheimer's disease and healthy control groups. However, statistical analysis on such 3-tissue compositions is not trivial: boundedness ($0 < T_W < 1\ ;\ 0 < T_G < 1\ ;\ 0 < T_C < 1$) and non-independence ($T_W + T_G + T_C = 1$) render traditional statistical analysis of the 3-tissue compositions inappropriate. Therefore, we adopted the Compositional Data Analysis (CoDA) framework (Aitchison, 1982; Pawlowsky-Glahn and Buccianti, 2011). To this end, we designed an isometric log-ratio transform (Egozcue et al., 2003) tailored to our 3-tissue compositions at hand:

$$ilr_1 = \frac{1}{\sqrt{6}} \times \log \frac{T_W{}^2}{(T_C \times T_G)}$$

$$ilr_2 = \frac{1}{\sqrt{2}} \times \log \frac{T_C}{T_G}$$

Unlike the original 3-tissue compositions themselves, which are bounded and non-independent, the isometric log-ratio transformed data

are free to range across all real numbers and are independent, resulting in only 2 degrees of freedom in the 3-tissue compositional space. Classical multivariate methods can then be applied to the log-ratio transformed data to perform statistical analysis (Martín-Fernández et al., 2015).

To determine if the 3-tissue profiles of different classes of WMH exhibited statistically significant differences, MANCOVAs were performed on the isometric log-ratio transformed data. Royston's tests of multivariate normality were used to assess the isometric log-ratio transformed data, and Mahalanobis distances used to detect any potential multivariate outliers. MANCOVAs were then performed between NAWM and each WMH class separately, as well as between each WMH class, both for periventricular and deep lesion types, and for distance-based lesion classes. Age, sex, intracranial volume and diagnostic group were included as covariates in the analyses. In addition, MANCOVAs were performed comparing WMH classes in Alzheimer's disease patients to healthy control participants, with age, sex and intracranial volume as covariates. Bonferroni corrections were applied within each analysis to correct for the multiple comparisons performed. Pillai's trace was used as the multivariate test in all analyses. All statistical analyses were carried out in the R (version 3.4.1).

2.8. Data availability statement

The data on which the findings of this study are based are available upon reasonable request from: (i) AIBL, for demographic and FLAIR data (from https://aibl.csiro.au/research/support); and (ii) corresponding author, for diffusion MRI data. The data are not publicly available due to ethical restrictions.

3. Results

3.1. Clinical and demographic characteristics

Clinical and demographic characteristics for the Alzheimer's disease and healthy control groups are summarised in Table 1. No significant differences were observed between groups for age, sex, or intracranial volume.

Table 1
Descriptive statistics.

	Alzheimer's disease (n = 48)	Healthy elderly controls (n = 94)	Statistics	p-value
Age, mean (SD) [range]	77.42 (8.3) [56.6–91.4]	78.12 (7.4) [57.7–93.2]	$t(140) = 0.75$	0.46
Males (%)	21 (43.8)	44 (46.8)	$\chi^2(1) = 0.03$	0.87
11C-PIB positivity (%)	48 (100)	31 (33)	$\chi^2(1) = 57.83$	<0.001
Intracranial volume (cm^3), mean (SD)	1402.95 (128.1)	1433.61 (134.8)	$t(140) = 1.30$	0.20
Total WMH volume (cm^3), mean (SD)	13.90 (13.3)	8.43 (9.4)	$t(71.4) = 2.54$	0.01
Regional WMH volumes (cm^3), mean (SD)				
Periventricular	12.81 (12.7)	7.54 (8.8)	$F(1,138) = 13.75$[a]	<0.001
Deep	1.09 (1.25)	0.89 (1.2)	$F(1, 138) = 14.69$[a]	<0.001
Region 1	2.61 (2.1)	2.32 (2.0)	$F(1, 138) = 1.38$[a]	0.24
Region 2	4.49 (3.4)	2.50 (2.6)	$F(1, 138) = 0.48$[a]	0.49
Region 3	6.72 (8.7)	3.57 (5.6)	$F(1, 138) = 24.06$[a]	<0.001

[a] Statistical analysis performed on cubic root transforms of WMH volume.

3.2. White matter hyperintensity volume

Total WMH volume was higher in Alzheimer's disease patients compared to control subjects, after controlling for age and intracranial volume ($F(1,138) = 13.75$, $P < 0.001$). Considering our two WMH classification schemes in turn: (a) No significant differences were observed between Alzheimer's disease and control groups for deep WMH volume ($F(1,138) = 1.38$, $P = 0.24$), while there was a significantly greater periventricular WMH volume in Alzheimer's disease patients compared to controls ($F(1,138) = 14.69$, $P < 0.001$). (b) Alzheimer's disease patients had a comparable load of WMH within Region 1 when compared to healthy elderly control subjects ($F(1,138) = 0.48$, $P = 0.49$). However, the WMH load in Region 2 and Region 3 was significantly higher in patients compared to controls (*Region 2*$F(1,138) = 24.06$, $P < 0.001$; *Region 3*: $F(1,138) = 14.81$, $P < 0.001$). Each of the above was compared between amyloid-positive and amyloid-negative healthy control subjects, but no significant differences were found in WMH volumes for any of these classes (see Table S1, Supplementary Material).

3.3. Comparing 3-tissue profiles of WMH classes

Fig. 3 shows the 3-tissue compartment maps of WMH in one participant. Further examples of the 3-tissue maps for other subjects are provided in the Supplementary Material (Fig. S2).

3.3.1. Periventricular vs deep WMH

As shown in the boxplots in Fig. 4, and ternary plot in Fig. 5, the 3-tissue profiles derived from SS3T-CSD showed different compositions of T_W, T_G, and T_C in periventricular and deep WMH, with higher T_C in periventricular WMH than in deep WMH. Periventricular and deep WMH formed distinct clusters based on their 3-tissue profiles alone, as did NAWM. The log-ratio transformed data is shown in Fig. 6, which exhibits the mean and 95% confidence ellipses of each group (WMH class or NAWM) in the 2-dimensional coordinate system, revealing the distinct clusters formed by each group. Statistical analysis using a MANCOVA showed significant differences between NAWM and periventricular WMH in terms of 3-tissue composition ($F(2, 277) = 5647.29$, $P < 0.001$, Pillai's trace = 0.976), between NAWM and deep WMH ($F(2, 274) = 1170.92$, $P < 0.001$, Pillai's trace = 0.895), and between periventricular and deep WMH ($F(2, 274) = 278.52$, $P < 0.001$, Pillai's trace = 0.670), after adjusting for age, sex, intracranial volume and diagnostic group. Differences in 3-tissue compositions were statistically significant at a Bonferroni corrected P-value of 0.017.

3.3.2. Distance-based region analysis

Fig. 7A shows a ternary plot exhibiting the 3-tissue profiles of WMH within three distance-based regions, defined by concentric distances from the lateral ventricles. As shown in the ternary plot, the different region classes of WMH again exhibited distinct 3-tissue profiles, and differed from NAWM. The log-ratio transformed data is shown in Fig. 7B. Multivariate tests using a MANCOVA, adjusting for age, sex, ICV, and diagnostic group showed a significant difference between NAWM and all three region classes (Region 1: $F(2, 277) = 8290.27$, $P < 0.001$, Pillai's trace = 0.984; Region 2: $F(2, 277) = 2551.93$, $P < 0.001$, Pillai's trace = 0.949; Region 3: $F(2, 277) = 1369.31$, $P < 0.001$, Pillai's trace = 0.908), as well as significant pairwise differences between each of the region classes themselves (Region 1 vs Region 2: $F(2, 277) = 556.72$, $P < 0.001$, Pillai's trace = 0.801; Region 1 vs Region 3: $F(2, 277) = 790.98$, $P < 0.001$, Pillai's trace = 0.851; Region 2 vs Region 3: $F(2, 277) = 56.94$, $P < 0.001$, Pillai's trace = 0.291), with a Bonferroni-corrected significant P-value of 0.008.

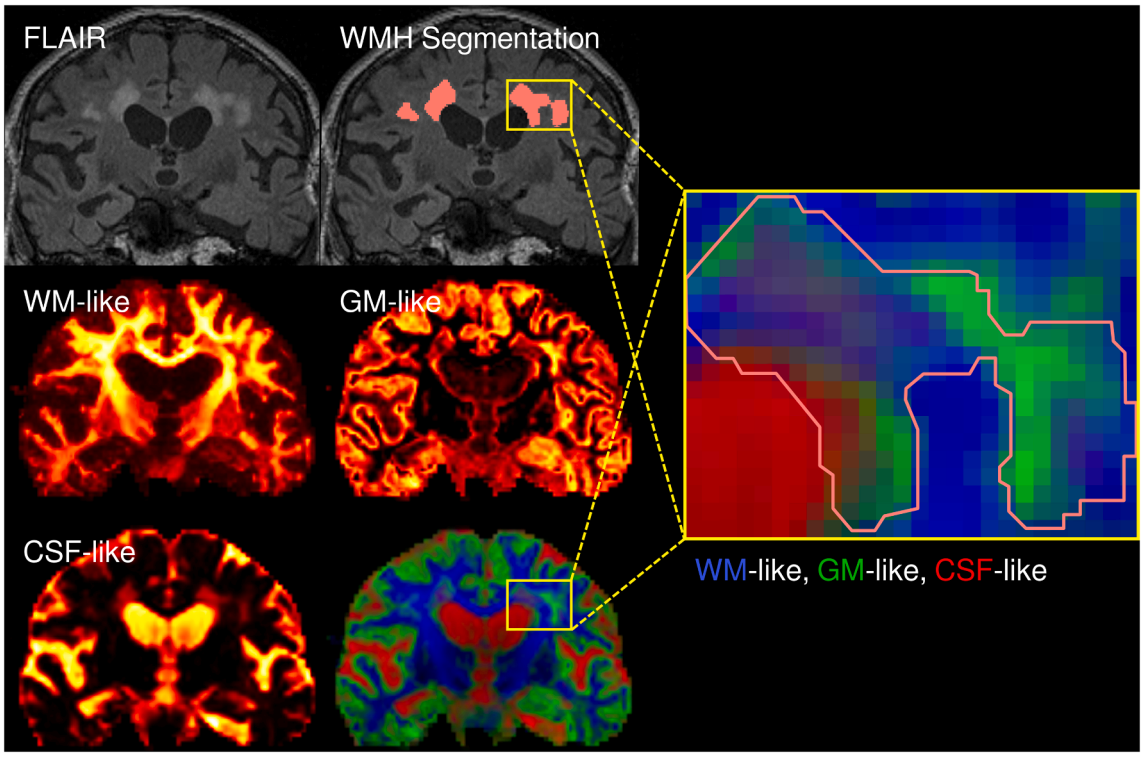

Fig. 3. Investigating *in vivo* microstructural heterogeneity of white matter hyperintensities using SS3T-CSD. WMH appear largely homogeneous on FLAIR MRI (top left), from which they can be segmented (segmentation shown on the FLAIR image on top right in pink). We computed the white matter-like (WM-like), grey matter-like (GM-like) and CSF-like signal compartments using single-shell, 3-tissue constrained spherical deconvolution (SS3T-CSD) (shown as heat maps in middle left, right, and bottom left, respectively). The three tissue compartments are shown in a single tissue-encoded colour map on the bottom right (WM-like = blue, GM-like = green, CSF-like = red). As can be seen in inset on the right, the region corresponding to WMH shows a heterogeneous mix of the three tissue compartments (segmentation outline shown in pink). (For interpretation of the references to colour in this figure legend, the reader is referred to the web version of this article.)

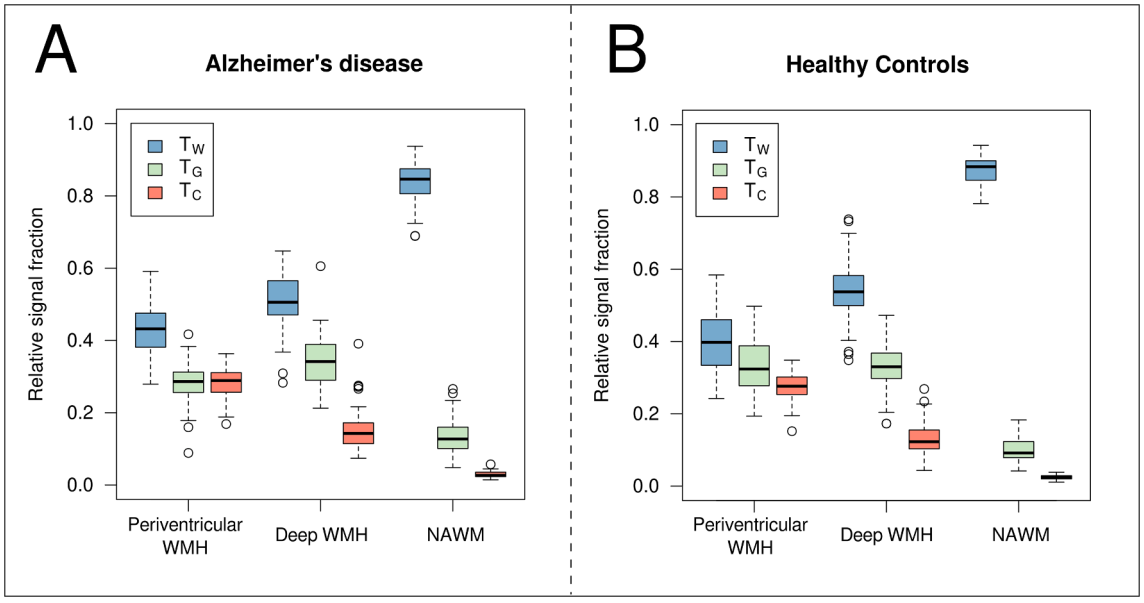

Fig. 4. Boxplots showing relative signal fractions within lesions and NAWM. The relative T_W, T_G, T_C signal fractions are displayed across all (A) Alzheimer's disease subjects ($n = 48$) and (B) healthy elderly control subjects ($n = 94$) as the median (line), first, and third quartiles (box) of the median (whiskers represent 1.5 interquartile range). Normal-appearing white matter (NAWM) exhibits high T_W fraction as expected, reflecting the high white matter-like diffusion profile with relatively low T_G and T_C fractions, both in healthy elderly and Alzheimer's disease subjects. In contrast, the WMH classes exhibit higher T_G and T_C fractions. Periventricular and deep WMH can be distinguished from one another by their relative signal fractions, and the two lesion types exhibit a similar profile in Alzheimer's disease patients as they do in control subjects.

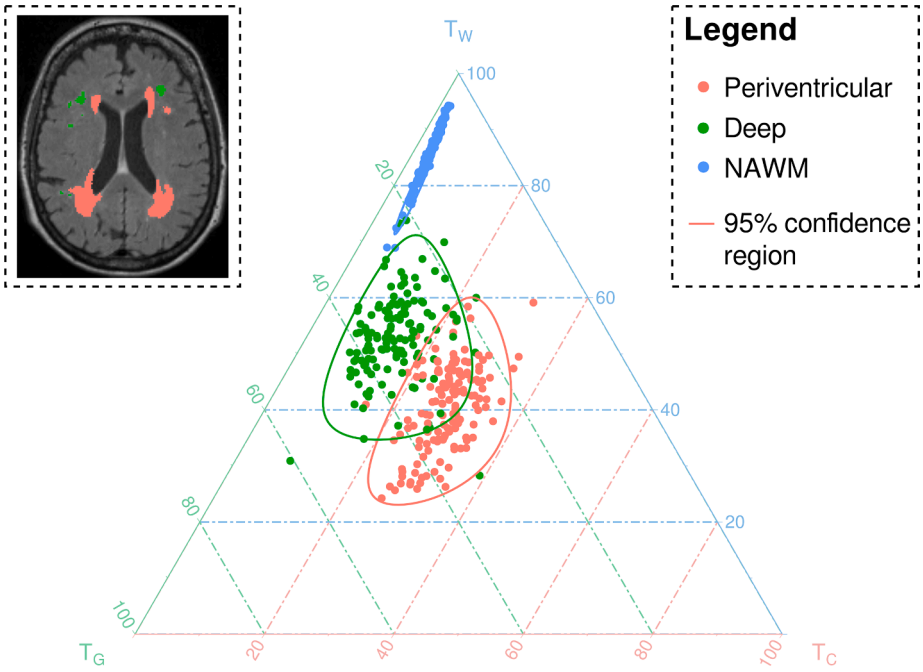

Fig. 5. Ternary plot exhibiting relative signal fractions within periventricular and deep lesions and NAWM. For each subject, the periventricular WMH, deep WMH, and NAWM are displayed on a ternary plot, with the location of the data point corresponding to the relative T_W, T_G and T_C fractions of the lesions (or NAWM) for that subject. Given the similarity in the profile of lesions in Alzheimer's disease subjects and controls, all subjects are included here. The relative tissue fraction is shown as a percentage along the left (T_W), right (T_G), and bottom (T_C) axes. Remarkably, the periventricular WMH, deep WMH, and NAWM appear in distinct clusters, exhibiting their different profiles with regard to relative tissue fractions obtained from the SS3T-CSD diffusion data. An example of the classification of lesions into periventricular and deep is shown in the inset. The 95% population confidence regions are plotted for each WMH class and NAWM.

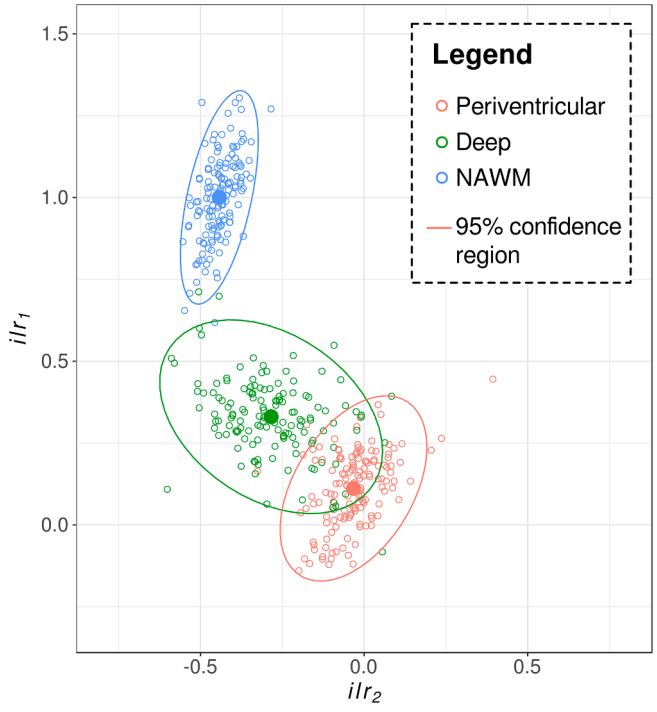

Fig. 6. Isometric log-ratio transformed diffusional data comparing periventricular WMH, deep WMH and NAWM. An isometric log-ratio (*ilr*) transform was applied to the relative signal fractions (T_W, T_G, T_C), to transform the compositional data into a two-coordinate system. The transformed data for the periventricular and deep WMH, and NAWM are shown here, and reflect the same data shown in Fig. 4. The centroid for each WMH class or NAWM is shown as a solid circle, while the solid line reflects the 95% population confidence ellipse for each class. Statistical analyses comparing the diffusional profile of lesion classes and NAWM was performed on this isometric log-ratio transformed data. Pairwise MANOVAs exhibited that there were statistically significant differences in the transformed data between the two lesion types, and between the lesions and NAWM. This could then be meaningfully back-transformed to interpret a significant difference in the mean diffusion profile between the two lesion types, and between the lesions and NAWM.

3.4. Comparing 3-tissue profiles in Alzheimer's disease and healthy controls

MANCOVAs were additionally performed to compare the 3-tissue profiles of WMH in Alzheimer's disease patients when compared to controls. Significant differences (at a Bonferroni-corrected p-value of 0.025) between the Alzheimer's disease and control groups were observed in the 3-tissue composition of periventricular lesions ($F(2, 136) = 10.68$, $P < 0.001$, Pillai's trace = 0.136) and to a lesser extent in deep lesions ($F(2, 133) = 4.82$, $P = 0.010$), Pillai's trace = 0.068), after accounting for age, sex, and intracranial volume. Comparing the three distance-based regions, significant differences were again observed between Alzheimer's disease patients and controls in the three lesion classes: Region 1 ($F(2, 136) = 15.61$, $P < 0.001$, Pillai's trace = 0.187); Region 2 ($F(2, 136) = 23.57$, $P < 0.001$, Pillai's trace = 0.257); and to a lesser extent in Region 3 ($F(2, 136) = 5.70$, $P = 0.004$, Pillai's trace = 0.077), at a Bonferroni-corrected p-value of 0.017). Ternary plots showing 3-tissue profiles of WMH lesion types in Alzheimer's disease and healthy controls are provided in the Supplementary Material (Fig. S3).

4. Discussion

In this study, we applied a novel diffusion MRI method to investigate *in vivo* microstructural characteristics of white matter hyperintensities in a cohort of healthy elderly and Alzheimer's disease subjects. We firstly demonstrate the ability of SS3T-CSD to probe microstructural heterogeneity within WMH, as previously exhibited (Dhollander et al, 2017). Investigation of different lesion classes demonstrated that different lesion types exhibit distinct 3-tissue profiles across our cohort. Moreover, in the context of Alzheimer's disease, we find that lesion classes in Alzheimer's disease patients exhibit subtly different 3-tissue profiles when compared to healthy controls. These findings suggest that the 3-tissue profiles utilised in this study could be used to probe WMH *in vivo* as heterogeneous entities, which could enable further investigation and understanding of their clinical and pathological association with Alzheimer's disease.

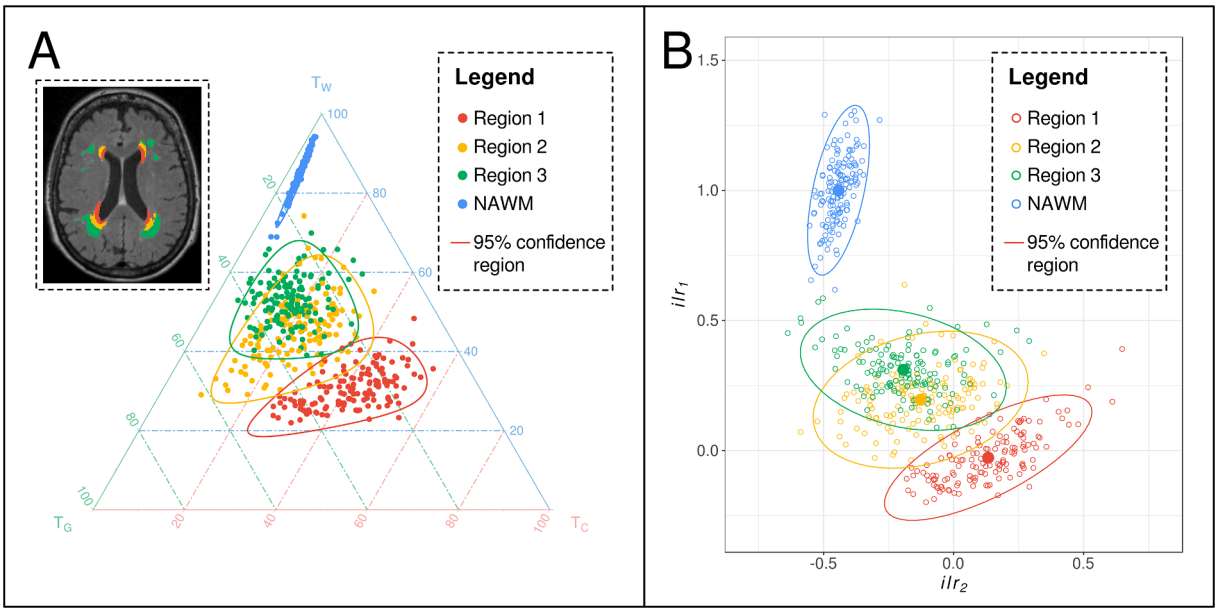

Fig. 7. Compositional data analysis of lesions in each distance-based region and NAWM. (A) As with Fig. 5, the relative T_W, T_G and T_C fraction for WMH or NAWM is displayed on a ternary plot. Each data point reflects the mean T_W, T_G and T_C fraction across all voxels falling within the NAWM mask (blue), or within one of three regions-of-interest (Regions 1, 2, and 3), located at concentric distances from the lateral ventricles, from a single subject. When looking across all subjects, the WMH falling within each region-of-interest exhibit a distinct diffusional profile, and the diffusional profile of each lesion area can be distinguished. The lines reflect the 95% confidence region or predictive region for each lesion region or NAWM. (B) An isometric log-ratio transform was applied to the relative signal fractions (T_W, T_G, T_C) to transform the compositional data into a two-coordinate system. Each data point reflects the transformed diffusion profile from a single subject, while the solid circle reflects the centroid and concentric solid line reflects the 95% population confidence ellipse for each lesion region or NAWM. Statistical analysis was performed on the isometric log-ratio transformed data, which showed significant pairwise differences in the diffusional profile between all regions, and between NAWM and each region. (For interpretation of the references to colour in this figure legend, the reader is referred to the web version of this article.)

4.1. 3-tissue profiles differentiate different WMH classes

WMH identified on FLAIR are commonly subdivided into different lesion classes; however, these lesion types are variable, and no gold standard classification scheme exists. Commonly, WMH are dichotomised into confluent periventricular and deep lesion subtypes, whereby lesions that are continuous with the lateral ventricles are distinguished from those that appear deeper within white matter with respect to the ventricles. Alternatively, distance-based classification schemes are used to distinguish lesion areas that are in the immediate periventricular (or juxtaventricular) zone, compared to those at further distances from the ventricles. Here, we probed two different classifications of WMH to determine whether different lesion types would exhibit different 3-tissue profiles.

Although the categorical distinction between periventricular and deep WMH is argued to be somewhat arbitrary (DeCarli et al., 2005), these two lesion classes have been suggested to have differing neuropathological substrates (Fazekas et al., 1991, 1993). As such, we hypothesised that confluent periventricular and deep lesions would exhibit different microstructural properties, and that these differences could be detected with diffusion MRI, despite appearing visually indistinguishable on FLAIR intensity. Indeed, our data indicate that these two lesion classes exhibit distinct 3-tissue profiles in our cohort of healthy elderly and Alzheimer's disease subjects. As shown in Fig. 4, the relative T_W-T_G-T_C compositions of periventricular and deep WMH across subjects could be clearly distinguished from one another.

Histologically, confluent periventricular lesions are characterised by substantial axonal and myelin loss and reactive gliosis, whereas punctate deep WMH have been reported to exhibit more mild changes with myelin loss (Fazekas et al., 1991, 1993; Schmidt et al., 2011a). In our work, the periventricular WMH exhibited distinctively higher T_C than NAWM and deep WMH. This suggests an increase in free water, given that the response function for T_C is derived from the diffusion signal in pure CSF voxels, and hence an increase in T_C reflects a shift towards properties resembling free diffusion. Such a finding is in line with prior histological work, as the substantial myelin and axonal loss that presumably arises within the periventricular lesions is likely accompanied by increased extracellular fluid (Weller, 1998). On the other hand, the 3-tissue profile of deep WMH across subjects suggests less severe damage: while it was clearly distinguishable from that of normal-appearing white matter, it was characterised by decreased T_W and relative increases both in T_G and T_C, rather than a marked increase in T_C specifically, as was observed in periventricular WMH. This suggests that disruption to white matter within these deep WMH may reflect less severe changes, in line with the mild myelin loss and gliosis that is histologically observed.

It should be noted, however, that heterogeneity in the 3-tissue profile of lesions could be observed *within* confluent periventricular lesions (Fig. 7) and as such, averaging the tissue profile over the whole lesion class could potentially fail to reflect variability in the microstructural changes within these continuous lesions. For instance, lesions within the immediate periventricular zone likely have distinguishable characteristics from large confluent hyperintensities (Sze et al., 1986; Fazekas et al., 1993; Schmidt et al., 2011a), despite potentially becoming continuous with them over time. The increased T_C observed in the periventricular lesions could have been driven by the increased interstitial fluid resulting from ependymal discontinuation in the immediate periventricular zone, and subsequent CSF leakage into the white matter, rather than being a characteristic of the whole confluent lesion. We were thus interested in extending the above analysis that was based on a periventricular/deep classification with a complementary investigation that probed the 3-tissue profile of lesion areas based on their distance from the lateral ventricles.

Here, we defined three regions-of-interest at set distances from the ventricles. While others have similarly used arbitrary distances to classify periventricular and deep WMH (Wen and Sachdev, 2004; DeCarli et al., 2005), we should highlight that our objective here was not to investigate different "classes" of lesions, but rather to determine if there were consistent, distance-related characteristics to WMH sub-regions

that would potentially reflect heterogeneity within confluent lesions. Our findings suggest that lesion areas within each distance band from the lateral ventricles indeed exhibited distinct microstructural characteristics. The high T_C observed in lesion regions falling within 10 mm of the lateral ventricles (within Region 1) suggests that WMH areas within this immediate periventricular zone have increased free fluid content when compared to NAWM. This could arise due to increased interstitial fluid as a consequence of partial loss of the ependymal lining, which is characteristic of periventricular lesions in elderly individuals (Fazekas et al., 1993).

Importantly, all WMH types were distinctively different in 3-tissue composition when compared to normal-appearing white matter across both healthy elderly subjects and Alzheimer's disease patients. NAWM across subjects had high T_W content as expected, reflecting a 3-tissue profile that was similar to healthy white matter. The observed distribution of NAWM profiles across subjects (Fig. 4) suggests that in some individuals, even non-lesional white matter was exhibiting signs of some pathological insult (though more subtle and likely widespread), which is as expected given our previous findings of substantial fibre tract degeneration in the Alzheimer's disease patients from the same cohort (Mito et al., 2018). Indeed, NAWM surrounding WMH has been shown in other studies to exhibit diffusional abnormalities (Maillard et al., 2014; Maniega et al., 2015; Maniega, 2018), contributing to a so-called WMH "penumbra" (Maillard et al., 2011).

4.2. 3-tissue profiles of WMH in Alzheimer's disease

In addition to comparing WMH across the whole cohort, we additionally investigated whether Alzheimer's disease patients exhibited distinct 3-tissue profiles in the same classes of WMH when compared to healthy control participants. Indeed, we found that 3-tissue profiles differed in Alzheimer's disease patients compared to controls, across all WMH classes, both when using periventricular and deep classifications, as well as using distance-based classifications. Differences in the 3-tissue profiles were more prominent in lesions confluent with (periventricular), or nearby (Regions 1 and 2) the ventricles, while lesions further from the ventricles (deep and Region 3) exhibited more subtle differences in Alzheimer's disease patients when compared to control participants. This may relate to differences in lesion volumes within different WMH classes, but could also potentially reflect subtle differences in underlying histopathology, for which histological validation would be required.

When considering WMH volumes, Alzheimer's disease patients in our cohort exhibited a significantly higher periventricular WMH volume when compared to healthy elderly subjects (Table 1). This is consistent with the increased severity of extensive periventricular hyperintensities that has been previously reported in Alzheimer's disease (Barber et al., 1999). Moreover, periventricular WMH, rather than deep WMH, have been preferentially associated with cognitive impairment and dementia (O'Brien et al., 1996; de Groot et al., 2002; Prins et al., 2004). As such, these lesions could be more deleterious than deep WMH, and more closely associated with Alzheimer's disease symptomatology (Fazekas et al., 1987). The 3-tissue profile of these lesions could thus itself be a useful reflection of more adverse underlying pathology, and could potentially provide an *in vivo* probe to distinguish more harmful, potentially disease-related changes, from benign age-related processes, regardless of the size, shape or location of a lesion.

On the other hand, when comparing distance-based classes the overall lesion volume within this most proximal distance band was comparable between healthy elderly individuals and Alzheimer's disease patients in our cohort, which suggests that lesions in this immediate periventricular area reflect more benign, age associated changes that likely arise due to their location in a potential watershed region. This appears to contradict the suggestion that in periventricular lesions (using the periventricular/deep WMH classification), a 3-tissue profile characterised by high T_C is indicative of deleterious underlying pathology due to there being a greater volume of periventricular lesions in Alzheimer's disease subjects than in controls. In fact, when lesion regions were classified according to distance from the ventricles irrespective of whether they were contiguous with other lesion regions, it was those regions falling within Regions 2 and 3 (which had distinctively lower T_C than those lesion region falling within 10 mm of the ventricles) that were greater in volume in Alzheimer's disease subjects than in controls.

These findings, though seemingly contradictory with the aforementioned findings using a periventricular/deep classification, suggest an important consequence: the use of conventional classification schemes (particularly distinguishing between periventricular and deep lesion types) could be misleading, as they do not take account of the substantial heterogeneity within white matter lesions. While the arbitrary nature of conventional classification schemes, and the importance of distinctions among different types of periventricular and deep WMH have previously been highlighted (DeCarli et al., 2005; Kim et al., 2008; Schmidt et al., 2011b), most research studies have adopted conventional classifications to probe disease-relevant associations.

Inferences are commonly made regarding the clinical relevance and pathological correlates of WMH based on these conventional classes, and could similarly be made from our own analysis above; however, careful consideration is required of the resultant findings given the aggregation of complex information into a single, oversimplified class. The use of three distance-based classes reveals that different conclusions can be drawn from the same data by investigating the lesions while considering the heterogeneity that may be present at different distance bands. Importantly, this highlights the pitfalls of using conventional classification schemes, particularly when investigating their relevance to disease. Indeed, we suggest that one should not consider how lesion types are associated to disease without considering their existing heterogeneity, which we propose can be investigated *in vivo* using this methodology.

4.3. Probing microstructure with diffusion MRI

In addition to identifying microstructural differences between WMH in different locations and classes, an important result of the present study was in establishing the feasibility of diffusion MRI, and particularly SS3T-CSD, in assessing and characterising within-lesion microstructural heterogeneity *in vivo*. As suggested above, the somewhat limited understanding of the contribution of WMH to Alzheimer's disease could stem from the simplistic way in which these lesions are commonly investigated *in vivo*, despite post-mortem evidence that they are pathologically complex. To this end, we suggest that the diffusion MRI characteristics of lesions could function as an *in vivo* probe, potentially in conjunction with FLAIR MRI, to investigate how WMH may contribute both clinically and pathologically to Alzheimer's disease.

Previous diffusion MRI research has attempted to investigate microstructural changes within WMH, by investigating these lesions using diffusion tensor imaging (DTI). These studies have investigated white matter mostly in terms of tensor metrics such as fractional anisotropy and/or mean diffusivity, and assessed how they may be altered in, or associated with WMH (de Groot et al., 2000; Firbank et al., 2003; Taylor et al., 2007; Vernooij et al., 2008; Lee et al., 2009; Topakian et al., 2010; Altamura et al., 2016; Seiler et al., 2018). Studies commonly report white matter microstructure, as measured using these DTI-derived metrics, to be altered not only within WMH (Bastin et al., 2009; Maniega et al., 2015), but additionally altered within NAWM in patients with such lesions (Firbank et al., 2003; Vernooij et al., 2008; Maniega et al., 2015). As such, DTI has been suggested to be a more sensitive model to assess subtle white matter damage than WMH detected on FLAIR (Charlton et al., 2010; Maillard et al., 2013). However, the diffusion tensor is a limited model that cannot adequately describe white matter microstructure in voxels containing more than

one fibre population (i.e., most white matter voxels) (Jeurissen et al., 2013; Jones et al., 2013), and changes to DTI metrics may be difficult to interpret in brain injury (Budde et al., 2011). Indeed, WMHs predominantly arise in crossing fibre regions around the lateral ventricles, the same regions in which tensor-based metrics are most difficult to interpret (see Supplementary Figure S4). DTI is unable to provide clear indication of the specific nature of microstructural damage within WMH, and differences quantified by tensor-based metrics can be inaccurate or misleading, even within normal appearing white matter. For example, FA is found to be very low in many voxels within the centrum semiovale region, despite the fibre tracts within this region being coherently oriented as evidenced both by brain dissection and by higher order modelling (Farquharson et al., 2013). Such effects of multiple crossing fibres can result in failure to detect damage to fibre tracts due to the already artifactually low anisotropy estimates based on FA values, or seemingly paradoxical increases in FA in abnormal regions resulting from selective reduction of one fibre population in a multi-fibre voxel (Groeschel et al., 2014). Such interpretational difficulties are likely to be exacerbated within more severely affected regions such as WMH. Although tensor-based metrics could be sensitised to differences in WMH classes, this does not resolve issues with the interpretability of DTI metrics (see Supplementary Figures S5–S7).

More recently, application of advanced, or multi-tissue diffusion MRI methods have enabled greater insight into microstructural changes, both in Alzheimer's disease, and in other neurological diseases. Techniques such as free water elimination, or neurite orientation dispersion and density imaging (NODDI) have been applied to investigate microstructural alterations in Alzheimer's disease (Colgan et al., 2016; Hoy et al., 2017; Ji et al., 2017), and to investigate white matter abnormalities in other neurological conditions (Billiet et al., 2014). Other methods of compartment modelling are also being developed that enable probing of white matter microstructure (Lampinen et al., 2020). Application of these biophysical models to investigate the microstructure of WMH could be insightful. Indeed, investigation of brain microstructure using advanced diffusion MRI methods has become an area of recent interest from which important advances are likely to be achieved (Alexander et al., 2019; Novikov et al., 2019).

In the present work, we utilised single-shell 3-tissue constrained spherical deconvolution (SS3T-CSD) to represent the diffusion MRI signal as a proxy to assess white matter microstructure (Dhollander and Connelly, 2016a; Dhollander et al., 2016). There are a number of advantages to this method that enable us to identify particular changes to white matter structures. SS3T-CSD is able to more appropriately model white matter in voxels that also contain other tissue types, by also modelling different tissue compartments in addition to white matter, as has been done for multi-shell data (Jeurissen et al., 2014). The added advantage of SS3T-CSD is that it can model 3 tissue compartments using single-shell data alone, enabling investigation of existing single-shell data without increasing acquisition requirements (Aerts et al., 2019). While we had high b-value single shell data available in this cohort, SS3T-CSD could also be valuable at lower b-values (Dimond et al., 2020; Newman et al., 2020).

In this study, we took into account joint changes to the complete 3-tissue composition: T_W, T_G, and T_C. This enabled us to characterise microstructural properties of tissue when it deviated from that of normal white matter. By characterising WMH in terms of these three signal fractions, we could interpret the resulting 3-tissue profile based on how alike the diffusion signal properties were to those derived from normal white matter, grey matter and CSF. This promising approach has similarly been adopted to investigate tissue heterogeneity in tumor regions using multi-shell CSD (Chamberland et al., 2019). However, careful consideration is required when interpreting the results, based on the context within which we observe changes to the 3-tissue composition. That is, we should not simply interpret increases or decreases in each signal fraction a reflection of alterations in the amount of healthy tissue type from which the response function was derived. For example, an increase in T_G, as was evident across WMH in comparison to NAWM, should not be interpreted as an increase in actual grey matter, but a shift toward something that has similar diffusion characteristics. This increase in T_G could be compatible with astrogliosis, as proliferation of glial cells is known to be a characteristic of WMH, and such a change would likely have a similar effect as grey matter on the diffusion signal: diffusion would still be relatively hindered, but much more isotropic than the healthy white matter represented by T_W. An increase in the T_C fraction could be interpreted as an increase in free fluid, which would likely reflect increases in interstitial fluid that may accompany nearby ependymal breakdown or local myelin or axonal loss (Dhollander et al, 2017). Moreover, we should highlight that the 3-tissue composition is tailored in this respect to investigate WMH, and further considerations should be taken in the context of other brain abnormalities and lesions (for example, within deep grey matter).

Importantly, a major advantage of characterising microstructure using this 3-tissue model, is that we could identify heterogeneity within WMH that cannot easily be identified *in vivo* using FLAIR. This enabled identification of clear variability across different classes of lesions, and even within confluent lesions that otherwise appeared largely homogeneous on FLAIR. Such a finding has major implications when investigating these lesions *in vivo*: on the evidence of a technique that enables identification of *in vivo* variability within lesions, it would appear inappropriate to amalgamate all WMH together as a singular pathological entity.

4.4. Limitations and future directions

This work represents a preliminary investigation into the *in vivo* heterogeneity of WMH that can be explored with diffusion MRI, and as such there are a number of limitations to this work that should be highlighted. Firstly, given that we do not have histological data to compare our *in vivo* metrics to, we cannot directly interpret the results in terms of their pathological basis. Direct interpretation of the tissue fractions described here – for instance, increases in a given fraction such as T_C – would require comparison with histopathology. However, it should be noted that, due to the large signal decay of the CSF response function, T_C is unlikely to reflect anything other than free water. As such, future work that correlates these diffusion metrics with post-mortem histopathology could provide more direct evidence for the specific histological underpinnings of these metrics, and enable broader *in vivo* investigation of disease-relevant pathology within WMH in large cohort studies.

Secondly, the aims of this study were to determine if we could probe *in vivo* variability within WMH using diffusion MRI, and to characterise different lesion areas based on their diffusional properties, but did not include the generation of a classification scheme. Our findings suggest that future work that characterises lesions based on their specific microstructural properties, rather than on arbitrary visually-guided or purely distance-based schemes, could enable the development of novel classification schemes with more meaningful microstructural basis. Such diffusion-based classification schemes could prove particularly valuable when investigating the association of WMH with disease-specific changes, given that certain microstructural changes are likely to be more detrimental than others.

Finally, while we explored the microstructural properties of WMH in healthy elderly individuals and Alzheimer's disease subjects, in this work, we did not focus on aspects specific to the microstructural characteristics of WMH in Alzheimer's disease. To this end, the development of the aforementioned, diffusion-based classification scheme in future work could be highly insightful, as it may enable us to identify the microstructural properties of more pathologically harmful WMH and determine and how these might be related to Alzheimer's disease.

4.5. Conclusion

In this study, we were able to detect microstructural heterogeneity within lesions *in vivo*, and identify variability within lesion classes based on their microstructural features through the application of a 3-tissue signal representation of diffusion MRI data. Diffusion MRI is more sensitive to underlying pathological features than FLAIR MRI, and would thus be a highly valuable probe to investigate WMH, potentially in conjunction with FLAIR. Given that Alzheimer's disease subjects have higher lesion load of certain classes and locations of WMH as well as subtly different diffusion profiles of WMH, it would be useful to investigate the particular *in vivo* features that are closely related with disease progression. Future work investigating the microstructural properties of WMH and their clinical and pathological correlates is likely to be highly insightful.

CRediT authorship contribution statement

Remika Mito: Conceptualization, Formal analysis, Investigation, Writing - original draft, Writing - review & editing. **Thijs Dhollander:** Conceptualization, Methodology, Software, Writing - review & editing. **Ying Xia:** Methodology, Resources. **David Raffelt:** Methodology, Software. **Olivier Salvado:** Methodology, Resources. **Leonid Churilov:** Conceptualization, Formal analysis. **Christopher C. Rowe:** Resources, Funding acquisition. **Amy Brodtmann:** Conceptualization, Supervision, Funding acquisition, Writing - review & editing. **Victor L. Villemagne:** Conceptualization, Supervision, Funding acquisition. **Alan Connelly:** Conceptualization, Supervision, Funding acquisition, Writing - review & editing.

Declaration of Competing Interest

The authors declare that they have no known competing financial interests or personal relationships that could have appeared to influence the work reported in this paper.

Acknowledgements

We thank the patients, researchers and clinicians involved in the Australian Imaging, Biomarkers, and Lifestyle study of ageing. The Florey Institute of Neuroscience and Mental Health acknowledges the strong support from the Victorian Government and in particular the funding from the Operational Infrastructure Support Grant. The authors acknowledge the facilities and scientific and technical assistance of the National Imaging Facility, a National Collaborative Research Infrastructure Strategy (NCRIS) capability, at the Florey Institute of Neuroscience and Mental Health.

Funding

We are grateful to the National Health and Medical Research Council (NHMRC) of Australia and the Victorian Government's Operational Infrastructure Support Program for their funding support. VV is supported by an NHMRC Research Fellowship (1046571). RM is supported by a Melbourne International Research Scholarship from the University of Melbourne and Yulgibar Alzheimer's Research Program Award.

Appendix A. Supplementary data

Supplementary data to this article can be found online at https://doi.org/10.1016/j.nicl.2020.102479.

References

Aerts, H., Dhollander, T., Marinazzo, D., 2019. Evaluating the performance of 3-tissue constrained spherical deconvolution pipelines for within-tumor tractography. bioRxiv 2019: 629873.
Aitchison, J., 1982. The statistical analysis of compositional data. J. R. Stat. Soc. Ser. B 44, 139–160.
Alexander, D.C., Dyrby, T.B., Nilsson, M., Zhang, H., 2019. Imaging brain microstructure with diffusion MRI: practicality and applications. NMR Biomed. 32.
Altamura, C., Scrascia, F., Quattrocchi, C.C., Errante, Y., Gangemi, E., Curcio, G., et al., 2016. Regional MRI diffusion, white-matter hyperintensities, and cognitive function in alzheimer's disease and vascular dementia. J. Clin. Neurol. 12, 201–208.
Andersson, J.L.R., Sotiropoulos, S.N., 2016. An integrated approach to correction for off-resonance effects and subject movement in diffusion MR imaging. Neuroimage 125, 1063–1078.
Avants, B.B., Tustison, N.J., Stauffer, M., Song, G., Wu, B., Gee, J.C., 2014. The Insight ToolKit image registration framework. Front. Neuroinform. 8, 44.
Barber, R., Scheltens, P., Gholkar, A., Ballard, C., McKeith, I., Ince, P., et al., 1999. White matter lesions on magnetic resonance imaging in dementia with Lewy bodies, Alzheimer's disease, vascular dementia, and normal aging. J. Neurol. Neurosurg. Psychiatry 67, 66–72.
Basser, P.J., Mattiello, J., LeBihan, D., 1994. MR diffusion tensor spectroscopy and imaging. Biophys. J. 66, 259.
Bastin, M.E., Clayden, J.D., Pattie, A., Gerrish, I.F., Wardlaw, J.M., Deary, I.J., 2009. Diffusion tensor and magnetization transfer MRI measurements of periventricular white matter hyperintensities in old age. Neurobiol. Aging 30, 125–136.
Le Bihan, D., Poupon, C., Amadon, A., Lethimonnier, F., 2006. Artifacts and pitfalls in diffusion MRI. J. Magn. Reson. Imaging An Off. J. Int. Soc. Magn. Reson. Med. 24, 478–488.
Billiet, T., Mädler, B., D'Arco, F., Peeters, R., Deprez, S., Plasschaert, E., et al., 2014. Characterizing the microstructural basis of "unidentified bright objects" in neurofibromatosis type 1: A combined in vivo multicomponent T2 relaxation and multi-shell diffusion MRI analysis. NeuroImage Clin. 4, 649–658.
Braffman, B.H., Zimmerman, R.A., Trojanowski, J.Q., Gonatas, N.K., Hickey, W.F., Schlaepfer, W.W., 1988. in MR: pathologic correlation with gross and histopathology. 2. Hyperintense white-matter foci in the elderl. Am. J. Roentgenol. 151, 559–566.
Brex, P.A., Parker, G.J.M., Leary, S.M., Molyneux, P.D., Barker, G.J., Davie, C.A., et al., 2000. Lesion heterogeneity in multiple sclerosis: a study of the relations between appearances on T1 weighted images, T1 relaxation times, and metabolite concentrations. J. Neurol. Neurosurg. Psychiatry 68, 627–632.
Brickman, A.M., Zahodne, L.B., Guzman, V.A., Narkhede, A., Meier, I.B., Griffith, E.Y., et al., 2015. Reconsidering harbingers of dementia: progression of parietal lobe white matter hyperintensities predicts Alzheimer's disease incidence. Neurobiol. Aging 36, 27–32.
Budde, M.D., Janes, L., Gold, E., Turtzo, L.C., Frank, J.A., 2011. The contribution of gliosis to diffusion tensor anisotropy and tractography following traumatic brain injury: validation in the rat using Fourier analysis of stained tissue sections. Brain 134, 2248–2260.
Chamberland, M., Iqbal, N.S., Rudrapatna, S.U., Parker, G., Tax, C.M.W., Staffurth, J., et al., 2019. Characterising tissue heterogeneity in cerebral metastases using multi-shell multi-tissue constrained spherical deconvolution. In: International Society for Magnetic Resonance in Medicine (ISMRM). Montreal.
Charlton, R.A., Schiavone, F., Barrick, T.R., Morris, R.G., Markus, H.S., 2010. Diffusion tensor imaging detects age related white matter change over a 2 year follow-up which is associated with working memory decline. J. Neurol. Neurosurg. Psychiatry 81, 13–19.
Coffey, C.E., Figiel, G.S., Djang, W.T., Weiner, R.D., 1990. Subcortical hyperintensity on magnetic resonance imaging: a comparison of normal and depressed elderly subjects. Am. J. Psychiatry 147, 187.
Colgan, N., Siow, B., O'Callaghan, J.M., Harrison, I.F., Wells, J.A., Holmes, H.E., et al., 2016. Application of neurite orientation dispersion and density imaging (NODDI) to a tau pathology model of Alzheimer's disease. Neuroimage 125, 739–744.
DeCarli, C., Fletcher, E., Ramey, V., Harvey, D., Jagust, W.J., 2005. Anatomical mapping of white matter hyperintensities (WMH): exploring the relationships between periventricular WMH, deep WMH, and total WMH burden. Stroke 36, 50–55.
Dhollander, T., Connelly, A., 2016a. A novel iterative approach to reap the benefits of multi-tissue CSD from just single-shell (+ b= 0) diffusion MRI data. 24th Int. Soc. Magn. Reson. Med. 24: 3010.
Dhollander, T., Connelly, A., 2016. Generating a T1-like contrast using 3-tissue constrained spherical deconvolution results from single-shell (or multi-shell) diffusion MR data. In: ISMRM Workshop on Breaking the Barriers of Diffusion MRI. Lisbon, Portugal. p. 6.
Dhollander, T., Mito, R., Raffelt, D., Connelly, A., 2019. Improved white matter response function estimation for 3-tissue constrained spherical deconvolution. Proc. Intl. Soc. Mag. Reson. Med. 555.
Dhollander, T., Raffelt, D., Connelly, A., 2016. Unsupervised 3-tissue response function estimation from single-shell or multi-shell diffusion MR data without a co-registered T1 image. Proc. Int. Soc. Magn. Reson. Med. Work. Break. Barriers Diffus. MRI 5.
Dhollander, T., Raffelt, D., Connelly, A., 2017. Towards interpretation of 3-tissue constrained spherical deconvolution results in pathology. 25th Int. Soc. Magn. Reson. Med. 25:1815.
Dhollander, T., Raffelt, D., Connelly, A., 2018. Accuracy of response function estimation algorithms for 3-tissue spherical deconvolution of diverse quality diffusion MRI data. In: International Society for Magnetic Resonance in Medicine (ISMRM). France, Paris, p. 1569.

Dimond, D., Rohr, C.S., Smith, R.E., Dhollander, T., Cho, I., Lebel, C., et al., 2020. Early childhood development of white matter fiber density and morphology. Neuroimage 210.
Egozcue, J.J., Pawlowsky-Glahn, V., Mateu-Figueras, G., Barcelo-Vidal, C., 2003. Isometric logratio transformations for compositional data analysis. Math. Geol. 35, 279–300.
Ellis, K.A., Bush, A.I., Darby, D., De Fazio, D., Foster, J., Hudson, P., et al., 2009. The Australian Imaging, Biomarkers and Lifestyle (AIBL) study of aging: methodology and baseline characteristics of 1112 individuals recruited for a longitudinal study of Alzheimer's disease. Int. Psychogeriatrics 21, 672–687.
Farquharson, S., Tournier, J.-D., Calamante, F., Fabinyi, G., Schneider-Kolsky, M., Jackson, G.D., et al., 2013. White matter fiber tractography: why we need to move beyond DTI. J. Neurosurg. 118, 1367–1377.
Fazekas, F., Chawluk, J.B., Alavi, A., Hurtig, H.I., Zimmerman, R.A., 1987. MR signal abnormalities at 1.5 T in Alzheimer's dementia and normal aging. Am. J. Roentgenol. 149, 351–356.
Fazekas, F., Kleinert, R., Offenbacher, H., Payer, F., Schmidt, R., Kleinert, G., et al., 1991. The morphologic correlate of incidental punctate white matter hyperintensities on MR images. Am. J. Neuroradiol. 12, 915–921.
Fazekas, F., Kleinert, R., Offenbacher, H., Schmidt, R., Kleinert, G., Payer, F., et al., 1993. Pathologic correlates of incidental MRI white matter signal hyperintensities. Neurology 43, 1683.
Firbank, M.J., Minett, T., O'Brien, J.T., 2003. Changes in DWI and MRS associated with white matter hyperintensities in elderly subjects. Neurology 61, 950–954.
Genc, S., Tax, C.M.W., Raven, E.P., Chamberland, M., Parker, G.D., Jones, D.K., 2020. Impact of b-value on estimates of apparent fibre density. bioRxiv.
Gouw, A.A., Seewann, A., Vrenken, H., Van Der Flier, W.M., Rozemuller, J.M., Barkhof, F., et al., 2008. Heterogeneity of white matter hyperintensities in Alzheimer's disease: post-mortem quantitative MRI and neuropathology. Brain 131, 3286–3298.
Groeschel, S., Tournier, J.-D., Northam, G.B., Baldeweg, T., Wyatt, J., Vollmer, B., et al., 2014. Identification and interpretation of microstructural abnormalities in motor pathways in adolescents born preterm. Neuroimage 87, 209–219.
de Groot, J.C., de Leeuw, F.-E., Oudkerk, M., Hofman, A., Jolles, J., Breteler, M.M.B., 2000. Cerebral white matter lesions and depressive symptoms in elderly adults. Arch. Gen. Psychiatry 57, 1071–1076.
de Groot, J.C., De Leeuw, F., Oudkerk, M., Van Gijn, J., Hofman, A., Jolles, J., et al., 2002. Periventricular cerebral white matter lesions predict rate of cognitive decline. Ann. Neurol. 52, 335–341.
Hamilton, N., 2018. ggtern: An Extension to 'ggplot2', for the Creation of Ternary Diagrams [Internet]. Available from: http://cran.r-project.org/package=ggtern.
Hoy, A.R., Ly, M., Carlsson, C.M., Okonkwo, O.C., Zetterberg, H., Blennow, K., et al., 2017. Microstructural white matter alterations in preclinical Alzheimer's disease detected using free water elimination diffusion tensor imaging. PLoS ONE 12.
Jeurissen, B., Leemans, A., Tournier, J., Jones, D.K., Sijbers, J., 2013. Investigating the prevalence of complex fiber configurations in white matter tissue with diffusion magnetic resonance imaging. Hum. Brain Mapp. 34, 2747–2766.
Jeurissen, B., Tournier, J.-D., Dhollander, T., Connelly, A., Sijbers, J., 2014. Multi-tissue constrained spherical deconvolution for improved analysis of multi-shell diffusion MRI data. Neuroimage 103, 411–426.
Ji, F., Pasternak, O., Liu, S., Loke, Y.M., Choo, B.L., Hilal, S., et al., 2017. Distinct white matter microstructural abnormalities and extracellular water increases relate to cognitive impairment in Alzheimer's disease with and without cerebrovascular disease. Alzheimers. Res. Ther. 9, 63.
Jones, D.K., 2010. Challenges and limitations of quantifying brain connectivity in vivo with diffusion MRI. Imaging Med. 2, 341–355.
Jones, D.K., Knösche, T.R., Turner, R., 2013. White matter integrity, fiber count, and other fallacies: the do's and don'ts of diffusion MRI. Neuroimage 73, 239–254.
Kim, K.W., MacFall, J.R., Payne, M.E., 2008. Classification of white matter lesions on magnetic resonance imaging in elderly persons. Biol. Psychiatry 64, 273–280.
Lampinen, B., Szczepankiewicz, F., Mårtensson, J., van Westen, D., Hansson, O., Westin, C., et al., 2020. Towards unconstrained compartment modeling in white matter using diffusion-relaxation MRI with tensor-valued diffusion encoding. Magn. Reson. Med. 84, 1605–1623.
Lee, D.Y., Fletcher, E., Martinez, O., Ortega, M., Zozulya, N., Kim, J., et al., 2009. Regional pattern of white matter microstructural changes in normal aging, MCI, and AD. Neurology 73, 1722–1728.
Lee, S., Viqar, F., Zimmerman, M.E., Narkhede, A., Tosto, G., Benzinger, T.L., et al., 2016. White matter hyperintensities are a core feature of Alzheimer's disease: Evidence from the dominantly inherited Alzheimer network. Ann Neurol 79, 929–939.
de Leeuw, F.-E., Cees de Groot, J., Oudkerk, M., Witteman, J.C.M., Hofman, A., van Gijn, J., et al., 2000. Aortic atherosclerosis at middle age predicts cerebral white matter lesions in the elderly. Stroke 31, 425–429.
Maillard, P., Carmichael, O., Harvey, D., Fletcher, E., Reed, B., Mungas, D., et al., 2013. FLAIR and diffusion MRI signals are independent predictors of white matter hyperintensities. Am. J. Neuroradiol. 34, 54–61.
Maillard, P., Fletcher, E., Harvey, D., Carmichael, O., Reed, B., Mungas, D., et al., 2011. White matter hyperintensity penumbra. Stroke 42, 1917–1922.
Maillard, P., Fletcher, E., Lockhart, S.N., Roach, A.E., Reed, B., Mungas, D., et al., 2014. White matter hyperintensities and their penumbra lie along a continuum of injury in the aging brain. Stroke 45, 1721–1726.
Maniega, S.M., Meijboom, R., Chappell, F.M., Hernández, M.M.C.V., Starr, J.M., Bastin, M.E., et al., 2018. Spatial Gradient of Microstructural Changes in Normal-Appearing White Matter in Tracts Affected by White Matter Hyperintensities in Older Age. bioRxiv 2018: 412064.
Maniega, S.M., Valdes Hernandez, M.C., Clayden, J.D., Royle, N.A., Murray, C., Morris, Z., et al., 2015. White matter hyperintensities and normal-appearing white matter integrity in the aging brain. Neurobiol. Aging 36, 909–918.
Manjón, J.V., Coupé, P., Raniga, P., Xia, Y., Desmond, P., Fripp, J., et al., 2018. MRI white matter lesion segmentation using an ensemble of neural networks and overcomplete patch-based voting. Comput. Med. Imaging Graph.
Martín-Fernández, J.A., Daunis i Estadella, J., Mateu i Figueras, G., 2015. On the interpretation of differences between groups for compositional data. SORT Stat. Oper. Res. Trans. 39 (2), 231–252.
McAleese, K.E., Walker, L., Graham, S., Moya, E.L.J., Johnson, M., Erskine, D., et al., 2017. Parietal white matter lesions in Alzheimer's disease are associated with cortical neurodegenerative pathology, but not with small vessel disease. Acta Neuropathol. 134, 459–473.
Mito, R., Raffelt, D., Dhollander, T., Vaughan, D.N., Tournier, J.-D., Salvado, O., et al., 2018. Fibre-specific white matter reductions in Alzheimer's disease and mild cognitive impairment. Brain 141, 888–902.
Newman, B.T., Dhollander, T., Reynier, K.A., Panzer, M.B., Druzgal, T.J., 2020. Test–retest reliability and long-term stability of three-tissue constrained spherical deconvolution methods for analyzing diffusion MRI data. Magn. Reson. Med.
Novikov, D.S., Fieremans, E., Jespersen, S.N., Kiselev, V.G., 2019. Quantifying brain microstructure with diffusion MRI: Theory and parameter estimation. NMR Biomed. 32.
O'Brien, J., Desmond, P., Ames, D., Schweitzer, I., Harrigan, S., Tress, B., 1996. A magnetic resonance imaging study of white matter lesions in depression and Alzheimer's disease. Br. J. Psychiatry 168, 477–485.
Pantoni, L., Garcia, J.H., 1997. Pathogenesis of leukoaraiosis a review. Stroke 28, 652–659.
Pantoni, L., Garcia, J.H., Gutierrez, J.A., 1996. Cerebral white matter is highly vulnerable to ischemia. Stroke 27, 1641.
Pawlowsky-Glahn, V., Buccianti, A., 2011. Compositional data analysis. Wiley Online Library.
Prins, N.D., van Dijk, E.J., den Heijer, T., Vermeer, S.E., Koudstaal, P.J., Oudkerk, M., et al., 2004. Cerebral white matter lesions and the risk of dementia. Arch. Neurol. 61, 1531–1534.
Raffelt, D., Tournier, J.-D., Fripp, J., Crozier, S., Connelly, A., Salvado, O., 2011. Symmetric diffeomorphic registration of fibre orientation distributions. Neuroimage 56, 1171–1180.
Raffelt, D., Tournier, J.-D., Rose, S., Ridgway, G.R., Henderson, R., Crozier, S., et al., 2012a. Apparent fibre density: a novel measure for the analysis of diffusion-weighted magnetic resonance images. Neuroimage 59, 3976–3994.
Raffelt, D., Tournier, J., Crozier, S., Connelly, A., Salvado, O., 2012b. Reorientation of fiber orientation distributions using apodized point spread functions. Magn. Reson. Med. 67, 844–855.
Rezek, D.L., Morris, J.C., Fulling, K.H., Gado, M.H., 1987. Periventricular white matter lucencies in senile dementia of the Alzheimer type and in normal aging. Neurology 37, 1365–1368.
Rowe, C.C., Bourgeat, P., Ellis, K.A., Brown, B., Lim, Y.Y., Mulligan, R., et al., 2013. Predicting Alzheimer disease with β-amyloid imaging: results from the Australian imaging, biomarkers, and lifestyle study of ageing. Ann. Neurol. 74, 905–913.
Scheltens, P., Barkhof, F., Leys, D., Pruvo, J.P., Nauta, J.J., Vermersch, P., et al., 1993. A semiquantative rating scale for the assessment of signal hyperintensities on magnetic resonance imaging. J. Neurol. Sci. 114, 7–12.
Scheltens, P., Barkhof, F., Valk, J., Algra, P.R., van der Hoop, R.G., Nauta, J., et al., 1992. White matter lesions on magnetic resonance imaging in clinically diagnosed Alzheimer's disease. Evidence for heterogeneity. Brain 115 (Pt 3), 735–748.
Schmidt, R., Fazekas, F., Kleinert, G., Offenbacher, H., Gindl, K., Payer, F., et al., 1992. Magnetic resonance imaging signal hyperintensities in the deep and subcortical white matter: a comparative study between stroke patients and normal volunteers. Arch. Neurol. 49, 825–827.
Schmidt, R., Grazer, A., Enzinger, C., Ropele, S., Homayoon, N., Pluta-Fuerst, A., et al., 2011a. MRI-detected white matter lesions: do they really matter? J. Neural Transm. 118, 673–681.
Schmidt, R., Scheltens, P., Erkinjuntti, T., Pantoni, L., Markus, H.S., Wallin, A., et al., 2004. White matter lesion progression A surrogate endpoint for trials in cerebral small-vessel disease. Neurology 63, 139–144.
Schmidt, R., Schmidt, H., Haybaeck, J., Loitfelder, M., Weis, S., Cavalieri, M., et al., 2011b. Heterogeneity in age-related white matter changes. Acta Neuropathol. 122, 171–185.
Seiler, S., Fletcher, E., Hassan-Ali, K., Weinstein, M., Beiser, A., Himali, J.J., et al., 2018. Cerebral tract integrity relates to white matter hyperintensities, cortex volume, and cognition. Neurobiol. Aging 72, 14–22.
Spilt, A., Goekoop, R., Westendorp, R.G.J., Blauw, G.J., de Craen, A.J.M., van Buchem, M.A., 2006. Not all age-related white matter hyperintensities are the same: a magnetization transfer imaging study. Am. J. Neuroradiol. 27, 1964–1968.
Van Straaten, E.C.W., Fazekas, F., Rostrup, E., Scheltens, P., Schmidt, R., Pantoni, L., et al., 2006. Impact of white matter hyperintensities scoring method on correlations with clinical data: the LADIS study. Stroke 37, 836–840.
Sze, G., De Armond, S.J., Brant-Zawadzki, M., Davis, R.L., Norman, D., Newton, T.H., 1986. Foci of MRI signal (pseudo lesions) anterior to the frontal horns: histologic correlations of a normal finding. Am. J. Roentgenol. 147, 331–337.
Taylor, W.D., Bae, J.N., MacFall, J.R., Payne, M.E., Provenzale, J.M., Steffens, D.C., et al., 2007. Widespread effects of hyperintense lesions on cerebral white matter structure. AJR Am. J. Roentgenol. 188, 1695–1704.
Topakian, R., Barrick, T.R., Howe, F.A., Markus, H.S., 2010. Blood-brain barrier permeability is increased in normal-appearing white matter in patients with lacunar stroke and leucoaraiosis. J. Neurol. Neurosurg. Psychiatry 81, 192–197.

Tournier, J.-D., Calamante, F., Connelly, A., 2007. Robust determination of the fibre orientation distribution in diffusion MRI: non-negativity constrained super-resolved spherical deconvolution. Neuroimage 35, 1459–1472.
Tournier, J.-D., Calamante, F., Gadian, D.G., Connelly, A., 2004. Direct estimation of the fiber orientation density function from diffusion-weighted MRI data using spherical deconvolution. Neuroimage 23, 1176–1185.
Tournier, J.-D., Smith, R.E., Raffelt, D.A., Tabbara, R., Dhollander, T., Pietsch, M., et al., 2019. MRtrix3: A fast, flexible and open software framework for medical image processing and visualisation. Neuroimage 551739.
Tustison, N.J., Avants, B.B., Cook, P.A., Zheng, Y., Egan, A., Yushkevich, P.A., et al., 2010. N4ITK: improved N3 bias correction. IEEE Trans. Med. Imaging 29, 1310–1320.
Veraart, J., Fieremans, E., Novikov, D.S., 2016. Diffusion MRI noise mapping using random matrix theory. Magn. Reson. Med.
Vernooij, M.W., de Groot, M., van der Lugt, A., Ikram, M.A., Krestin, G.P., Hofman, A., et al., 2008. White matter atrophy and lesion formation explain the loss of structural integrity of white matter in aging. Neuroimage 43, 470–477.
Weller, R.O., 1998. Pathology of cerebrospinal fluid and interstitial fluid of the CNS: significance for Alzheimer disease, prion disorders and multiple sclerosis. J. Neuropathol. Exp. Neurol. 57, 885–894.
Wen, W., Sachdev, P., 2004. The topography of white matter hyperintensities on brain MRI in healthy 60-to 64-year-old individuals. Neuroimage 22, 144–154.
Young, V.G., Halliday, G.M., Kril, J.J., 2008. Neuropathologic correlates of white matter hyperintensities. Neurology 71, 804–811.
Zhang, Y., Brady, M., Smith, S., 2001. Segmentation of brain MR images through a hidden Markov random field model and the expectation-maximization algorithm. IEEE Trans. Med. Imaging 20, 45–57.